

Earth's inner core: innermost inner core or hemispherical variations?

K.H. Lythgoe^{a,*}, A. Deuss^a, J.F. Rudge^a, J.A. Neufeld^{a,b,c}

^a*Bullard Laboratories, Department of Earth Sciences, Madingley Road, Cambridge, CB3 0EZ, UK*

^b*BP Institute, Madingley Road, Cambridge, CB3 0EZ, UK*

^c*Department of Applied Mathematics and Theoretical Physics, Centre for Mathematical Sciences, Wilberforce Road, Cambridge, CB3 0WA, UK*

Abstract

The structure of Earth's deep inner core has important implications for core evolution, since it is thought to be related to the early stages of core formation. Previous studies have suggested that there exists an innermost inner core with distinct anisotropy relative to the rest of the inner core. Using an extensive new data set of hand-picked absolute travel time observations of the inner core phase PKIKP, we find that the data are best explained by variations in anisotropy between two hemispheres and do not require an innermost inner core. We demonstrate that observations of an innermost inner core are an artifact from averaging over lateral anisotropy variations. More significantly we show that hemispherical variations in anisotropy, previously only imaged in the upper inner core, continue to its centre. The eastern region has 0.5-1.5%

*Corresponding author

Email address: kh143@cam.ac.uk; +441223337180 (K.H. Lythgoe)

anisotropy, whereas the western region has 3.5-8.8% anisotropy increasing with depth, with a slow direction at 57-61° to the Earth's rotation axis at all depths. Such anisotropy is consistent with models of aligned hcp or bcc iron aggregates.

Keywords: Earth's inner core, seismology, anisotropy, body waves

1. Introduction

Since velocity anisotropy in the inner core was first proposed (Morelli et al., 1986; Woodhouse et al., 1986), with a fast direction parallel to Earth's rotation axis and a slow direction perpendicular to it, reports of increasing complexity in the structure of the inner core have continued. Degree 1 lateral variations in anisotropy have been imaged with both body waves (Tanaka and Hamaguchi, 1997; Creager, 1999; Niu and Wen, 2001; Garcia, 2002; Waszek et al., 2011; Irving and Deuss, 2011) and normal modes (Deuss et al., 2010). The western 'hemisphere' has stronger anisotropy than the eastern, and also appears to be slower, at least in the upper 100 km (Niu and Wen, 2001; Wen and Niu, 2002; Waszek et al., 2011). Hemispheres have been imaged up to 600-700 km below the inner core boundary (Creager, 1999; Sun and Song, 2008; Irving and Deuss, 2011; Tanaka, 2012), although there is some disagreement about the exact location of hemisphere boundaries.

More recently, a region of distinct anisotropy at the centre of the inner core has been reported (Ishii and Dziewonski, 2002). This apparent innermost inner core (IMIC) has greater anisotropy than the rest of the inner core and a slow direction that is no longer perpendicular to Earth's rotation axis. However, there is no consistent image of the IMIC, with its radius and slow

20 direction differing between models (Ishii and Dziewonski, 2002; Beghein and
21 Trampert, 2003; Cormier and Stroujkova, 2005; Cao and Romanowicz, 2007;
22 Sun and Song, 2008; Niu and Chen, 2008).

23 Ishii and Dziewonski (2002) originally suggested the existence of an IMIC,
24 with a radius of 300 km and a slow direction at 45° to Earth's rotation axis.
25 Using normal mode splitting, Beghein and Trampert (2003) subsequently
26 updated the IMIC radius to 400 km and the slow direction to being parallel
27 to Earth's spin axis. Waveform analysis by Cormier and Stroujkova (2005)
28 found no evidence for a sharp IMIC and concluded that if an IMIC were to
29 exist it would need to have a radius of at least 500 km, with a transition
30 region of at least 100 km. Cao and Romanowicz (2007) reported that if an
31 IMIC is present, it most likely has a radius of 500 km and a slowest direction
32 at 55° to Earth's rotation axis. Lastly, Sun and Song (2008) find an IMIC
33 radius of 590 km, although their study cannot be used to test for its existence,
34 since an IMIC is hard-wired into the model.

35 Here we present a new, high quality body wave data set and use it to
36 study anisotropy in the deep inner core. Specifically we investigate the depth
37 extent of hemispherical variations and test if the existence of an innermost
38 inner core is actually required by the seismic data.

39 **2. Data and Methods**

40 We use the inner core compressional body wave phase, PKIKP, to in-
41 vestigate the deep inner core, since normal modes have no sensitivity to the
42 centre of the Earth and are unable to image sharp boundaries. Many pre-
43 vious inner core studies have measured the arrival time of PKIKP - which

44 travels through the mantle, outer and inner core (Figure 1a) - with respect
 45 to a reference phase traversing only the mantle and outer core (PKPbc or
 46 PKPab), in order to remove the effect of mantle heterogeneity and source
 47 mislocation (Creager, 1999; Irving and Deuss, 2011). PKPbc arrives at epi-
 48 central distances less than 155.5° , so PKPbc-PKIKP data is only sensitive to
 49 the upper 350 km of the inner core. Additionally at large epicentral distances
 50 (hence large inner core depths) PKIKP and the reference phase, PKPab, have
 51 very different paths in the mantle and so differences in travel time between
 52 the two phases cannot be attributed to the inner core alone. We therefore
 53 study absolute travel times of PKIKP, without a reference phase. Past stud-
 54 ies of absolute PKIKP travel times have used data from the International
 55 Seismological Centre (Ishii and Dziewonski, 2002; Su and Dziewonski, 1995),
 56 which despite being a large data set is noisy and may miss anomalous ar-
 57 rivals. Therefore, we prefer to use our own handpicked measurements to
 58 ensure that our data set is of the highest quality.

59 We have assembled a data set of ~ 2360 high-quality, handpicked absolute
 60 PKIKP arrival times, the largest yet used to study the inner core. We use
 61 events with a moment magnitude (M_w) greater than 6 for the time period
 62 1990-2008, for which the EHB catalogue (Engdahl et al., 1998) is available,
 63 providing accurate relocated event hypocentres and origin times. When tar-
 64 getting polar paths, we lowered the magnitude threshold to $M_w > 5$ in order
 65 to obtain more data. To ensure that PKIKP can be easily identified, source-
 66 receiver epicentral distances of 150° - 180° are used, corresponding to ray
 67 turning depths of less than 1010 km radius. We pick the onset of PKIKP
 68 arrivals and so are unaffected by waveform broadening due to inner core

69 attenuation.

70 The arrival time of PKIKP is measured with respect to the predicted
71 arrival time from the 1D Earth model AK135 (Figure 1b, Kennett et al.,
72 1995) and is corrected for ellipticity (Dziewonski and Gilbert, 1976). To
73 reduce the effect of mantle heterogeneity, we apply mantle corrections using
74 a global P-wave model (Li et al., 2008). Since PKIKP travels vertically in the
75 mantle, relatively little travel time signature is obtained from the mantle. We
76 also compare our results for the top of the inner core to differential travel time
77 studies, where the studied region overlaps, to confirm that there is minimal
78 mantle influence. We assume that the outer core is seismically homogeneous,
79 since it is vigorously convecting and previous seismic studies have found no
80 heterogeneity (Souriau et al., 2003; Ishii and Dziewonski, 2005).

81 We investigate anisotropy by analysing travel time as a function of ray
82 angle with Earth’s rotation axis in the inner core. Following Creager (1992),
83 we parametrise weak cylindrical anisotropy as a perturbation to a spherically
84 symmetric model by

$$\frac{\delta t}{t} = -\frac{\delta v}{v} = a + b \cos^2 \zeta + c \cos^4 \zeta, \quad (1)$$

85 where v is the P-wave velocity in the reference model, δv is the velocity
86 perturbation, t is the time the ray spends in the inner core, δt is our measured
87 travel time residual and ζ is the angle between the ray path in the inner core
88 and Earth’s rotation axis. In this form a represents the difference between
89 the observed equatorial velocity and the reference model and b and c describe
90 the anisotropic variation of travel time with ζ . We define rays with $\zeta \leq 35^\circ$
91 as polar rays and $\zeta > 35^\circ$ as equatorial rays.

92 The total anisotropy (δv_{ani}) is defined as the difference between purely

93 polar ($\zeta=0^\circ$) and purely equatorial ($\zeta=90^\circ$) rays, i.e.

$$\delta v_{\text{ani}} = b + c, \quad (2)$$

94 while the average isotropic velocity perturbation (δv_{iso}) is found by averaging
95 over all ray angles

$$\delta v_{\text{iso}} = a + \frac{b}{3} + \frac{c}{5}. \quad (3)$$

96 We invert our observed travel times (δt) for parameters a , b and c from
97 equation 1, using a linear least squares inversion without damping. We
98 parametrise the model into discrete layers in order to avoid smoothing any
99 depth variations and trace the rays through the layers and hemispheres to
100 obtain the anisotropic and isotropic perturbations for each layer and hemi-
101 sphere.

102 Earlier studies of inner core hemispherical variations have attributed a
103 ray's travel time anomaly to one hemisphere only, based on the turning lo-
104 cation of the ray (Tanaka and Hamaguchi, 1997; Creager, 1999; Niu and
105 Wen, 2001; Garcia, 2002; Waszek et al., 2011; Irving and Deuss, 2011). How-
106 ever this method does not account for time the ray has spent in the other
107 hemisphere, which becomes more important at depth since ray paths are long
108 and tend to travel through both hemispheres. Therefore our tomographic ray
109 tracing technique is more precise in resolving lateral variations, especially at
110 depth, since we correctly attribute parts of each ray to the corresponding
111 hemisphere.

112 Sun and Song (2008) applied body wave tomography of the inner core
113 to PKP differential travel times. However the model of Sun and Song (2008)
114 cannot be used to investigate the existence of an IMIC since its radius is

115 defined a priori, along with the location of hemisphere boundaries. Here, we
 116 vary the location of the boundaries to find the solution that best fits the data.
 117 Differential travel times are also known to become increasingly unreliable as
 118 epicentral distance - hence inner core depth - increases, because the reference
 119 phase PKPab spends more time in the strongly heterogeneous D'' layer. As
 120 part of their study, Sun and Song (2008) investigate the difference between
 121 their quasi-3D method and a 1D ray tracing method and find very little
 122 difference between the two approaches.

123 Anisotropy in the IMIC has been defined as having a slowest direction
 124 which is no longer in the equatorial plane ($\zeta_{\text{slow}}=90^\circ$), with estimated slow
 125 angles (ζ_{slow}) ranging from 0° (Beghein and Trampert, 2003) to 55° (Cao
 126 and Romanowicz, 2007) from the rotation axis, with other intermediate val-
 127 ues (Ishii and Dziewonski, 2002; Sun and Song, 2008). These earlier studies
 128 visually assessed the slowest direction, but we quantify it analytically by
 129 finding the maximum of equation 1. We do this by differentiating equation 1
 130 with respect to ζ

$$\frac{d(\delta t/t)}{d\zeta} = -2 \cos(\zeta) \sin(\zeta) (b + 2c \cos^2(\zeta)) \quad (4)$$

131 which is zero at

$$\zeta_{\text{slow}} = \cos^{-1} \sqrt{\frac{-b}{2c}}. \quad (5)$$

132 We quantify how significant this slow direction is by subtracting the model
 133 predicted travel time residual at the slowest angle from the predicted travel
 134 time residual for a purely equatorial ray ($\zeta=90^\circ$).

135 We use an L2 misfit to assess how well the model matches our data

$$L2 = \frac{1}{N} \sum_{i=1}^N (\delta t_{\text{obs}} - \delta t_{\text{pred}})_i^2 \quad (6)$$

136 where N is the number of rays, δt_{obs} is the observed travel time residual and
 137 δt_{pred} is the model predicted travel time residual. Model uncertainties have
 138 been estimated from cross-validation, whereby a random 10% of the data
 139 is removed and a new model obtained. This is repeated 10 times with a
 140 different data subset removed each time, such that each data point is absent
 141 from one model. We compare the resulting 10 models to the initial model in
 142 order to quantitatively measure model fit and uncertainty.

143 We also want to compare our observed seismological anisotropy to pre-
 144 dicted anisotropy for mineral physics models of iron at inner core conditions.
 145 These models are quantified by the elastic parameters C_{ij} . Following Mat-
 146 tesini et al. (2010) and Stixrude and Cohen (1995), P-wave velocity for a
 147 single crystal of hcp iron with cylindrical symmetry, or for a bcc aggregate
 148 with symmetry axis at (1 1 1), can be expressed as

$$v_p = \left(\frac{1}{\rho} (C_{11} + (4C_{44} + 2C_{13} - 2C_{11}) \cos^2(\zeta) + (C_{33} + C_{11} - 4C_{44} - 2C_{13}) \cos^4(\zeta)) \right)^{\frac{1}{2}}. \quad (7)$$

149 where ρ is density. Equation 7 is valid for hexagonal close-packed (hcp) iron
 150 with cylindrical symmetry or for a body-centred-cubic (bcc) aggregate with
 151 symmetry axis at (1 1 1). Assuming that all crystals are aligned in one
 152 direction, the travel time residual can be approximated by

$$\frac{\delta t}{t} = - \frac{\delta v_p}{v_{p0}} \quad (8)$$

153 where v_{p0} is the Voigt average velocity and $\delta v_p = v_p - v_{p0}$.

3. Results

Our data set has good global coverage, with ~ 2250 equatorial paths ($\zeta > 35^\circ$, Figure 2a) and ~ 110 polar paths ($\zeta \leq 35^\circ$, Figure 2b). Unlike differential travel time studies, our polar paths are not dominated by South Sandwich Island events. Equatorial travel time residuals range from -2 to 6 seconds (Figure 2a, 2c) and so arrive late on average, indicating that equatorial rays generally travel slower than predicted by AK135. Conversely polar residuals range from -9 to 4 seconds (Figure 2b, 2d), so polar rays generally travel faster than predicted by AK135. Polar paths also display large longitudinal variations, with anomalously fast polar paths travelling the inner core between approximately 150°W and 40°E longitude (Figure 2d).

We firstly examine global inner core anisotropy without allowing for hemispherical variations (Figure 3). Our whole data set as a function of ζ is shown in Figure 3a. Figures 3b and c show the model resulting from the inversion for an inner core separated into three depth layers, with boundaries at 750 km and 550 km radius. Allowing for global anisotropy reduces our model misfit by 34% (Table 1) compared to no anisotropy. The model explains the data well for each layer (Figures 3d, e and f), with the resulting a , b and c values given in Table 1.

We find that anisotropy increases with depth, from around 2% at the top of the inner core to over 5% in the centre (Figure 3b). The predicted anisotropy curves (i.e. equation 1) for the top two layers (blue curves, Figure 3g) show cylindrical anisotropy, with polar rays travelling faster than equatorial rays. However at a radius of less than 550 km (orange curve, Figure 3g) the form of anisotropy changes to having a slowest angle at $\sim 56^\circ$ to

179 the rotation axis (Figure 3h). The slowest angle becomes more ‘significant’
 180 the more its travel time residual differs from that in the equatorial direction,
 181 thus the slow angle of the top two layers is ‘insignificant’, while the bottom
 182 layer is ‘significant’ (Figure 3i).

183 Anisotropy also increases with depth using a polynomial depth parametri-
 184 sation, but there is less constraint on the depth at which the form of anisotropy
 185 changes. We have varied the thickness of the deepest layer in our inversion
 186 and found the thickness of the apparent IMIC to be 550 ± 50 km. The
 187 base of the top layer at a radius of 750 km is effectively arbitrary but is
 188 chosen to equally distribute data across the three layers and demonstrates
 189 that anisotropy increases gradually with depth. Comparing our results with
 190 previous studies, we find that our laterally-averaged model is consistent with
 191 the presence of an IMIC at 550 km radius (Cormier and Stroujkova, 2005;
 192 Cao and Romanowicz, 2007).

193 However previous IMIC studies have not accounted for hemispherical vari-
 194 ations, which have been extensively imaged in the upper inner core. We
 195 would like to investigate if these two properties can be reconciled. We again
 196 invert our data for parameters a , b and c (equation 1) for 3 layers, but now
 197 allowing for variation between two hemispheres. The location of the hemi-
 198 sphere boundaries is varied systematically in a grid search, in order to find
 199 the boundaries with the lowest misfit (Figure 4a). The best-fitting bound-
 200 aries are at -95°W and 40°E , with a further misfit reduction of 15% compared
 201 to the model with no hemispherical variations (Table 1). We also perform
 202 a statistical F-test and conclude that this misfit reduction is significant, at
 203 99% confidence level, given the increased number of model parameters.

204 The location of the eastern boundary is consistent with that of all previous
 205 studies (Figure 4b; Tanaka and Hamaguchi, 1997; Creager, 1999; Garcia,
 206 2002; Niu and Wen, 2001; Waszek et al., 2011; Irving and Deuss, 2011),
 207 while the western boundary is located further eastwards than other studies
 208 have observed (Figure 4c). However it should be noted that past studies are
 209 only sensitive to the upper inner core (≥ 600 km radius). Although there
 210 is some variation in the travel time residual of polar paths between -95°
 211 and -150° (Figure 2d), most paths are not anomalous and so the anisotropy
 212 boundary is placed at -95° and not further westwards. This explains why
 213 the western boundary has a broad minimum with a higher uncertainty and
 214 indicates several possibilities: that the boundary is not sharp, has some
 215 depth variability or that it cannot be resolved accurately with present data
 216 coverage.

217 Figure 5 shows the resulting models for the eastern and western hemi-
 218 spheres, using the same layered parametrisation as in our global model (Fig-
 219 ure 3) and the lowest misfit boundary locations (Figure 4). Anisotropy
 220 throughout the entire eastern hemisphere is small, ranging from 0.5 to 1.5 %,
 221 with little variation of travel time with ray angle in any layer (Figure 5a-c).
 222 The slight variation that does exist is very small, especially given errors in
 223 the inversion. The eastern hemisphere generally has a slowest angle at 90°
 224 to the rotation axis (Figure 5d). The bottom layer has a slow direction at
 225 51° to the rotation axis, but has a large associated error ($\pm 13^\circ$) and there
 226 is only a very small difference between $\delta t/t$ for the slowest angle and 90°
 227 (Figure 5e).

228 Conversely the western hemisphere has large anisotropy that increases

229 with depth, from 3.5% in the top layer to 8.8% in the deepest layer (Figure 5f-
 230 h). A slow direction at $57\text{-}61^\circ$ is seen throughout the western hemisphere
 231 (Figure 5i), but slowness appears to become more significant with depth as
 232 anisotropy increases (Figure 5J). Hence, a slowest direction at intermediate
 233 angles is already present for a radius larger than 550 km and we do not
 234 require the presence of an innermost inner core. It should be noted that
 235 the sharp changes with depth seen in the western hemisphere are artifacts of
 236 inverting for discrete layers and it is likely that the increase in anisotropy is
 237 smoother.

238 To exclude any bias in the upper layers from rays travelling through the
 239 central layer, the same inversion is performed using short distance data that
 240 sample the top two layers only. In this instance anisotropy in the top layers
 241 doesn't change, showing that the stronger anomalies of deeper ray paths do
 242 not influence the upper layers. Moving the western boundary towards -180° ,
 243 to be consistent with previous studies, also has little effect on the resulting
 244 anisotropy model, because the western boundary is only constrained by a
 245 few polar paths. The hemisphere model still has the lowest misfit and again
 246 there is no need for an innermost inner core.

247 4. Discussion

248 4.1. Innermost inner core versus hemispherical variations

249 A change in slow direction from 90° to an intermediate angle in the deep
 250 inner core, was previously thought to be evidence of an IMIC (Figure 6a; Ishii
 251 and Dziewonski, 2002). However no past studies accounted for hemispherical
 252 variations and therefore averaged over eastern and western hemispheres. At

greater depths, ray paths are longer and tend to travel through both hemispheres, so the change in slow direction becomes apparent in the averaged model at depth, as seen in Figure 3. This may explain why different studies find differing IMIC depths. Consequently by properly accounting for hemispherical variations we find no evidence for an IMIC and, more significantly, we show that hemispheres continue to the centre of the Earth (see Figure 6b for a schematic of hemispherical structure). Therefore we demonstrate that the IMIC is an artifact from averaging over the two hemispheres.

Isotropic velocities in our models are similar to AK135 in both hemispheres, implying that the hemispheres have a similar composition. Hemispherical differences arise from anisotropy and we show that anisotropy is confined to a western hemisphere ‘wedge’ between -95°W and 40°E . However the sharpness of hemisphere boundaries, particularly the western boundary, cannot be accurately resolved with present data coverage, since there are few polar paths in this region.

Since we are studying travel times, we have no constraints on attenuation and do not exclude a change in attenuation with depth, as seen by Cormier and Li (2002) and Li and Cormier (2002). Although Li and Cormier (2002) found no obvious hemispherical differences in attenuation, this should be analysed further since the change in attenuation with depth may be confined to one hemisphere only.

4.2. Interpretation

We have found that the slowest direction at intermediate angles is a feature of the whole western hemisphere and is not confined to an IMIC. We now want to see if this form of anisotropy is consistent with predictions from

278 mineral physics. To do this, we calculate the predicted seismic anisotropy
 279 curves for several mineral physical models of iron at inner core conditions
 280 using equation 7 and assuming that all hcp crystals are aligned in one direc-
 281 tion. In Figure 7 we compare our observed seismic anisotropy to models of
 282 hcp iron aggregates with the fast axis aligned with Earth’s spin axis (Stixrude
 283 and Cohen, 1995; Steinle-Neumann et al., 2001; Vocablo et al., 2009; Mat-
 284 tesini et al., 2010; Sha and Cohen, 2010; Martorell et al., 2013) and a model of
 285 a cylindrically averaged bcc iron aggregate with 25% of its [111] axes aligned
 286 with the spin axis (Mattesini et al., 2010). For most hcp models the [001]
 287 axis is fastest (Stixrude and Cohen, 1995; Mattesini et al., 2010; Sha and
 288 Cohen, 2010; Martorell et al., 2013), so this axis is aligned along Earth’s spin
 289 axis. However for some hcp models this axis is slow and therefore has been
 290 rotated to lie in the equatorial plane (i.e. for models by Steinle-Neumann
 291 et al., 2001; Vocablo et al., 2009).

292 All mineral physics models predict some anisotropy, so are inconsistent
 293 with the small amount of observed eastern hemisphere anisotropy. Signifi-
 294 cantly all models predict a slowest direction at intermediate angles - ranging
 295 from 49° to 59° to the rotation axis (Mattesini et al., 2010; Steinle-Neumann
 296 et al., 2001) - and so qualitatively match western hemisphere anisotropy
 297 (Figure 7).

298 In the western hemisphere, most models underestimate the difference be-
 299 tween equatorial and polar velocities (Stixrude and Cohen, 1995; Vocablo
 300 et al., 2009; Mattesini et al., 2010; Sha and Cohen, 2010; Martorell et al.,
 301 2013). The models of Stixrude and Cohen (1995) and Steinle-Neumann et al.
 302 (2001) have slow directions at 56° and 59° to the rotation axis respectively,

303 matching the seismically observed slow direction. bcc iron (Mattesini et al.,
304 2010) matches deep anisotropy for polar angles, but not for equatorial an-
305 gles. The model of Steinle-Neumann et al. (2001) is the only model to predict
306 sufficient anisotropy to match the seismic observations.

307 There is much variation between published mineral physics models, with
308 no model completely matching seismically observed anisotropy. This is un-
309 surprising given the difficulty in recreating the conditions of the inner core -
310 all models are at incorrect pressures or temperatures and light elements are
311 not accounted for. It is also reasonable to assume that texturing in the inner
312 core is more complex than we analyse here. Nevertheless, all models agree
313 on the slowest angle not being perpendicular to the rotation axis.

314 Since all iron models are qualitatively consistent with western hemisphere
315 anisotropy, this implies that the western hemisphere is textured, with crys-
316 tals orientated along Earth's rotation axis. Increasing anisotropy with depth
317 implies that the degree of texturing also increases. Conversely eastern hemi-
318 sphere anisotropy shows no correlation with any model, suggesting that crys-
319 tals are randomly aligned. We must therefore look for a mechanism that will
320 generate a wedge of aligned crystals with a longitude width of $\sim 135^\circ$ and
321 with the degree of alignment increasing with depth.

322 Translation of the inner core, whereby the whole inner core moves in
323 one direction resulting in melting and crystallisation on opposite sides, is
324 one proposed mechanism (Monnereau et al., 2010; Alboussiere et al., 2010).
325 However many parts of this mechanism are unclear, primarily the actual
326 process that causes crystals to align. Furthermore translation requires a high
327 inner core viscosity which is relatively unconstrained, with possible values

328 varying by several orders of magnitude..Recent estimates of core thermal
329 conductivity are high (Pozzo et al., 2012) and so for translation to occur it
330 must be compositionally rather than thermally driven (Deguen et al., 2013;
331 Gubbins et al., 2013).

332 Alternatively variations in heat flow at the core-mantle boundary from
333 mantle convection, may extend to the inner core boundary (ICB) causing het-
334 erogeneous crystallisation rates (Aubert et al., 2011), and even melting (Gub-
335 bins et al., 2011). Calkins et al. (2012) recently showed that topography at the
336 core-mantle boundary could cause significant longitudinal variations in heat
337 flow along the ICB. These mechanism requires textural development from so-
338 lidification processes, such as alignment with Earth’s magnetic field (Karato,
339 1993) or dendritic solidification (Bergman, 1997). Yoshida et al. (1996) pro-
340 pose that anisotropy develops from topographic relaxation due to differential
341 crystallisation rates between the equator and pole. If crystallisation rates
342 vary in localised regions, this could feasibly generate localised regions of
343 anisotropy.

344 5. Conclusions

345 Using our extensive new data set of PKIKP travel time observations, we
346 show that hemispherical variations extend throughout the entire inner core,
347 with a strongly anisotropic western hemisphere and a weakly anisotropic east-
348 ern. A slow direction at 57° - 61° is seen throughout the western hemisphere
349 and is also required in models of bcc and hcp iron at core conditions. However
350 there is significant variation between mineral physics models and no model
351 provides a complete match to our seismic observations. We further show that

352 previous observations of an innermost inner core at the centre of the Earth
353 result from averaging over lateral variations and that an innermost inner core
354 is not required by our data. Our observation of distinct hemispheres at all
355 depths poses an intriguing problem: how to generate degree 1 asymmetry
356 throughout the entire inner core.

357 6. Acknowledgements

358 We would like to thank Xanwei Sha for making his results for hcp Fe at
359 core conditions available to us and Simon Redfern for discussions about min-
360 eral physics. We also thank Vernon Cormier and an anonymous reviewer for
361 helpful suggestions. K.H.L and A.D. are funded by the European Research
362 Council under the European Community's Seventh Framework Programme
363 (FP7/2007-2013)/ERC grant scheme number 204995. Data was downloaded
364 from IRIS DMC and figures made using GMT (Wessel and Smith, 1998).

365 Alboussiere, T., Deguen, R., Melzani, M., 2010. Melting-induced stratifica-
366 tion above the Earth's inner core due to convective translation. *Nature* 466,
367 744 – 747.

368 Aubert, J., Amit, H., Hulot, G., Olson, P., 2011. Thermochemical flows
369 couple the Earth's inner core growth to mantle heterogeneity. *Nature* 454,
370 758 – 761.

371 Beghein, C., Trampert, J., 2003. Robust normal mode constraints on inner
372 core anisotropy from model space search. *Science* 299, 552 – 555.

373 Bergman, M. I., 1997. Measurements of elastic anisotropy due to solidification

374 texturing and the implications for the Earth's inner core. *Nature*389, 60 –
375 63.

376 Calkins, M. A., Noir, J., Eldredge, J. D., Aurnou, J. M., 2012. The effects of
377 boundary topography on convection in Earth's core. *Geophys. J. Int.*189,
378 799 – 814.

379 Cao, A., Romanowicz, B., 2007. Test of the innermost inner core models
380 using broadband PKIKP travel time residuals. *Geophys. Res. Lett.*34, 1 –
381 5.

382 Cormier, V. F., Li, X., 2002. Frequency dependent attenuation in the inner
383 core. 2. A scattering interpretation. *J. Geophys. Res.*107, 2374.

384 Cormier, V. F., Stroujkova, A., 2005. Waveform search for the innermost
385 inner core. *Earth Planet. Sci. Lett.*236, 96 – 105.

386 Creager, K. C., 1992. Anisotropy of the inner core from differential travel
387 times of the phases PKP and PKIKP. *Nature*356, 309 – 314.

388 Creager, K. C., 1999. Large-scale variation in inner core anisotropy. *J. Geo-*
389 *phys. Res.*104, 23127 – 23139.

390 Deguen, R., Alboussiere, T., Cardin, P., 2013. Thermal convection in Earth's
391 inner core with phase change at its boundary. *Geophys. J. Int.*In press.

392 Deuss, A., Irving, J. C. E., Woodhouse, J. H., 2010. Regional variation of
393 inner core anisotropy from seismic normal mode observations. *Science*328,
394 1018 – 1020.

395 Dziewonski, A. M., Gilbert, F., 1976. The effect of small aspherical perturba-
 396 tions on travel times and a re-examination of the corrections for ellipticity.
 397 Geophys. J. R. astr. Soc.44, 7 – 17.

398 Engdahl, E. R., van der Hilst, R., Buland, R., 1998. Global teleseismics
 399 earthquake relocation with improved times and procedures for depth de-
 400 termination. Bull. Seismol. Soc. Am.88, 722 – 743.

401 Garcia, R., 2002. Constraints on upper inner core structure from waveform
 402 inversion of core phases. Geophys. J. Int.150, 651 – 664.

403 Gubbins, D., Alfe, D., Davies, C. J., 2013. Compositional instability of
 404 Earth’s solid inner core. Geophys. Res. Lett.40, 1084 – 1088.

405 Gubbins, D., Sreenivasan, B., Mound, J., Rost, S., 2011. Melting of the
 406 Earth’s inner core. Nature473, 361 – 363.

407 Irving, J. C. E., Deuss, A., 2011. Hemispherical structure in inner core ve-
 408 locity anisotropy. J. Geophys. Res.116, 1 – 17.

409 Ishii, M., Dziewonski, A. M., 2002. The innermost inner core of the earth:
 410 Evidence for a change in anisotropic behaviour at the radius of about
 411 300km. PNAS 99, 14026 –14030.

412 Ishii, M., Dziewonski, A. M., 2005. Constraints on the outer-core tangent
 413 cylinder using normal mode splitting measurements. Geophys. J. Int.162,
 414 787 – 792.

415 Karato, S., 1993. Inner core anisotropy due to the magnetic field - induced
 416 preferred orientation of iron. Science262, 1708 – 1711.

417 Kennett, B. L. N., Engdahl, E. R., Buland, R., 1995. Constraints on seismic
418 velocities in the Earth from traveltimes. *Geophys. J. Int.*122, 108 – 124.

419 Li, C., van der Hilst, R. D., Burdick, S., 2008. A new global model for P
420 wave speed variations in Earth’s mantle. *Geophys. Geochem. Geosys.*9, 1
421 – 21.

422 Li, X., Cormier, V. F., 2002. Frequency-dependent seismic attenuation in
423 the inner core. 1. A viscoelastic interpretation. *J. Geophys. Res.*107, 2361–
424 2374.

425 Martorell, B., Brodholt, J., Wood, I. G., Vocadlo, L., 2013. The ef-
426 fect of nickel on properties of iron at the conditions of Earth’s inner
427 core: Ab initio calculations of seismic wave velocities of Fe-Ni alloys.
428 *Earth Planet. Sci. Lett.*365, 143 – 151.

429 Mattesini, M., Belonoshko, A., Bufo, E., Ramirez, M., Simak, S., Udias,
430 A., Mao, H., Ahuja, R., 2010. Hemispherical anisotropic patterns of the
431 Earth’s inner core. *Proc. Natl. Acad. Sci. USA*107, 9507 – 9512.

432 Monnereau, M., Calvet, M., Margerin, L., Souriau, A., 2010. Lopsided growth
433 of the Earth’s inner core. *Science*328, 1014 – 1017.

434 Morelli, A., Dziewonski, A. M., Woodhouse, J. H., 1986. Anisotropy of the
435 inner core inferred from PKIKP travel times. *Geophys. Res. Lett.*13, 1545
436 – 1548.

437 Niu, F., Chen, Q. F., 2008. Seismic evidence for distinct anisotropy in the
438 innermost inner core. *Nature Geosci.*1, 692 – 696.

439 Niu, F., Wen, L., 2001. Hemispherical variations in seismic velocity at the
440 top of Earth's inner core. *Nature* 410, 1081 – 1084.

441 Pozzo, M., Davies, C., Gubbins, D., Alf, D., 2012. Thermal and electrical
442 conductivity of iron at Earth's core conditions. *Nature* 485, 355 – 358.

443 Sha, X., Cohen, R. E., 2010. First-principles thermal equation of state and
444 thermoelasticity of hcp Fe at high pressures. *Physical Review* 81, 1 – 10.

445 Souriau, A., Testem, A., Chevrot, S., 2003. Is there any structure inside the
446 liquid outer core? *Geophys. Res. Lett.* 30, 1567.

447 Steinle-Neumann, G., Stixrude, L., Cohen, R. E., Gulseren, O., 2001. Elas-
448 ticity of iron at the temperature of the Earth's inner core. *Nature* 413, 57
449 – 60.

450 Stixrude, L., Cohen, R. E., 1995. High-pressure elasticity of iron and
451 anisotropy of the Earth's inner core. *Science* 267, 1972 – 1975.

452 Su, W., Dziewonski, A., 1995. Inner core anisotropy in 3 dimensions. *J. Geo-*
453 *phys. Res.* 100, 9831 – 98952.

454 Sun, X., Song, X., 2008. The inner inner core of Earth: Texturing of iron crys-
455 tals from three-dimensional seismic anisotropy. *Earth Planet. Sci. Lett.* 269,
456 56 – 65.

457 Tanaka, S., 2012. Depth extent of hemispherical inner core from PKP(df)
458 and PKP(Cdiff) for equatorial paths. *Phys. Earth Planet. Inter.* 210, 50 –
459 62.

460 Tanaka, S., Hamaguchi, H., 1997. Degree one heterogeneity and hemispher-
461 ical variation of anisotropy in the inner core from PKP(BC)-PKP(DF)
462 times. *J. Geophys. Res.*102, 2925 – 2938.

463 Vocadlo, L., Dobson, D., Wood, I., 2009. Ab initio calculations of the
464 elasticity of hcp-fe as a function of temperature at inner-core pressure.
465 *Earth Planet. Sci. Lett.*288, 534 – 538.

466 Waszek, L., Irving, J., Deuss, A., 2011. Reconciling the hemispherical struc-
467 ture of the Earth’s inner core with its super-rotation. *Nature Geosci.*4, 264
468 – 267.

469 Wen, L., Niu, F., 2002. Seismic velocity and attenuation structures in the
470 top if the Earth’s inner core. *J. Geophys. Res.*107, 2273.

471 Wessel, P., Smith, W. H. F., 1998. New, improved version of generic mapping
472 tools released. *Eos Trans. AGU*79, 579.

473 Woodhouse, J. H., Giardini, D., Li, X. D., 1986. Evidence for inner core
474 anisotropy from free oscillations. *Geophys. Res. Lett.*13, 1549 – 1552.

475 Yoshida, S., Sumita, I., Kumazawa, M., 1996. Growth model of the inner
476 core coupled with outer core dynamics and the resulting elastic anisotropy.
477 *J. Geophys. Res.*101, 28085 – 28103.

Table 1: a , b and c values in each depth layer for three models: without anisotropy and hemispherical variations; with anisotropy but without hemispherical variations; with anisotropy and hemispherical variations. Misfits for each model are also given.

Model	Radius	a	b	c	Misfit (s^2)
No anisotropy		0	0	0	1.43
Anisotropy	>750 km	-0.0048	-0.0036	0.0215	0.95
	750 - 550 km	-0.0008	-0.0089	0.0420	
	<550 km	0.0070	-0.0950	0.1503	
Hemispheres - East	>750 km	-0.0043	0.0040	0.0099	0.81
	750 - 550 km	-0.0025	0.0336	-0.0220	
	<550 km	0.0060	-0.0213	0.0264	
	West	>750 km	-0.0062	-0.0308	0.0658
		750 - 550 km	0.0049	-0.0836	0.1423
		<550 km	0.0067	-0.1318	0.2194

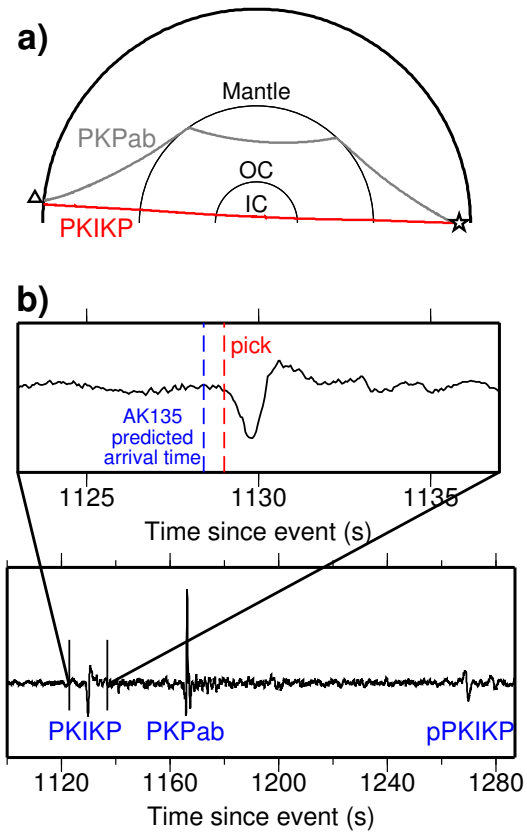


Figure 1: **a)** Ray paths of PKIKP (red) and PKPab (grey) through the Earth for an event-receiver epicentral distance of 180° . **b)** Example seismogram, showing the PKIKP arrival and predicted arrival time for AK135. Seismogram is for an event on 22nd September 2006 in Argentina ($M_w 6$) recorded at HIA station in northern China.

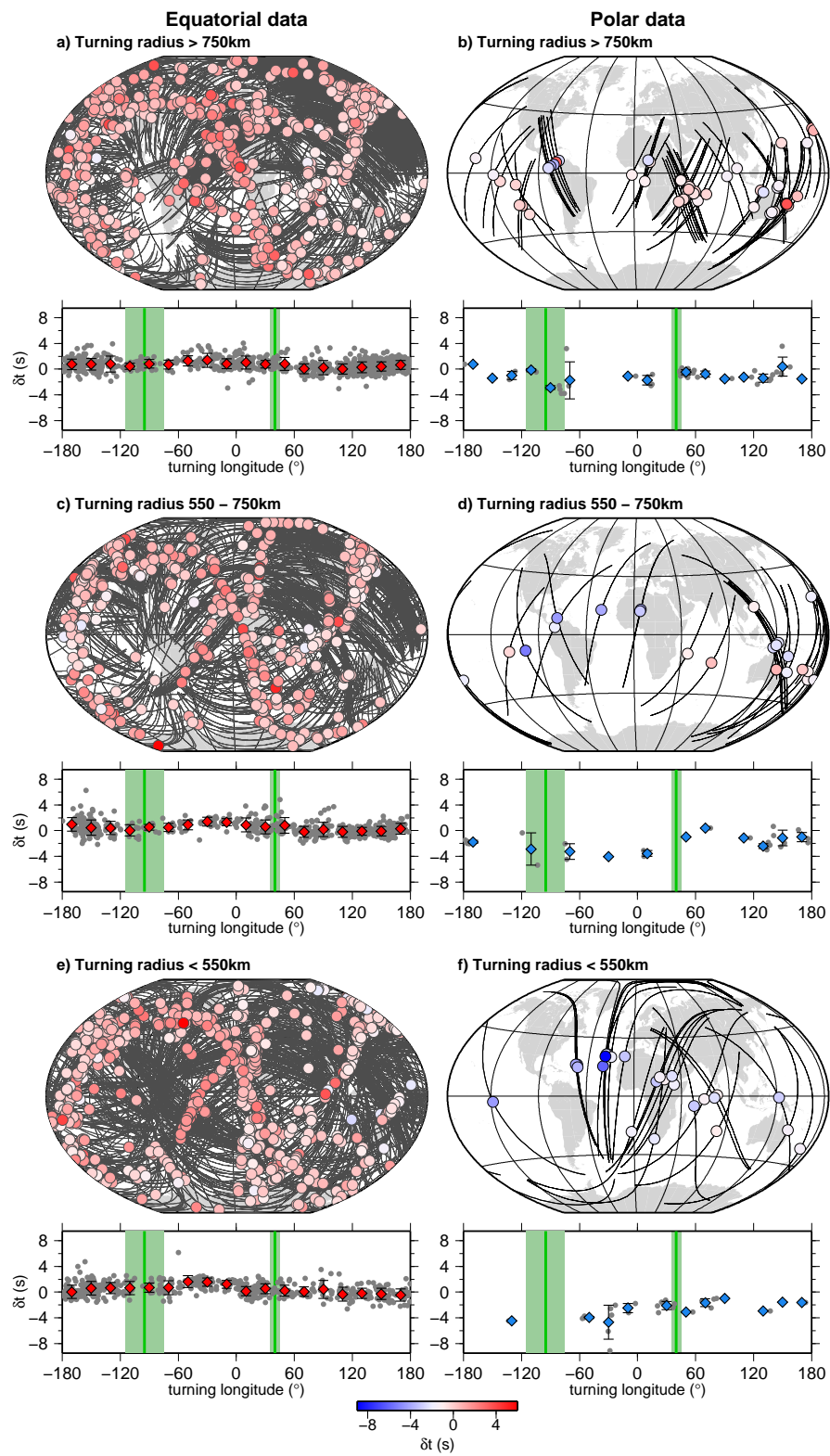


Figure 2: PKIKP travel time residuals, corrected for ellipticity and mantle heterogeneity, for equatorial (**a,c,e**) and polar paths (**b,d,f**) and separated according to ray turning point radius: greater than 750 km radius (**a,b**); between 550 km and 750 km radius (**c,d**); less than 550 km radius (**e,f**). Top panels show residuals in map form, plotted at the turning point with inner core ray paths plotted as black lines. Bottom panels show residuals as a function of turning point longitude (grey dots).

Red/blue diamonds show average residuals over 20° longitude bins, with error bars plotted as one standard deviation. Green lines show minimum misfit hemisphere boundary locations from Figure 4 with shading for cross-validation errors.

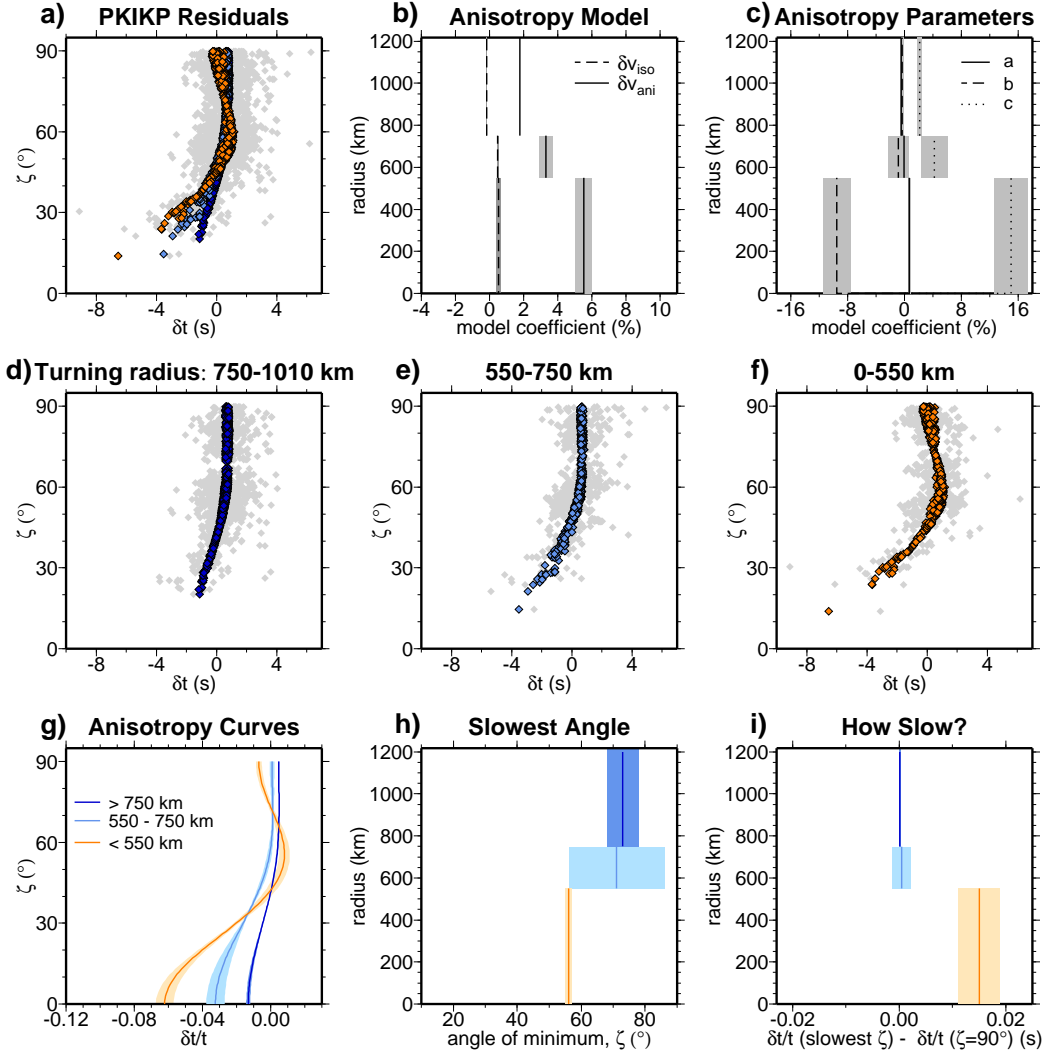


Figure 3: Results of inversion without allowing for hemispherical variations. **a)** Observed PKIKP travel time residuals (grey) with model predicted travel time residuals, coloured corresponding to ray turning depth: dark blue = turning in top layer, light blue = turning in middle layer, red = turning in bottom layer. **b)** Isotropic (dashed) and anisotropic (solid line) variations with respect to AK135. **c)** Model values for a , b and c (equation 1). Observed residuals (grey) and model predicted residuals (dark blue) for rays that turn between **d)** 750-1010 km radius, **e)** 550-750 km radius and **f)** less than 550 km radius. **g)** Anisotropy curves for $\delta t/t$ in each layer. **h)** ζ for which the anisotropy curve is maximum (the slowest angle). **i)** Difference between $\delta t/t$ for the slowest angle and the equatorial direction ($\zeta = 90^\circ$). Shaded regions show errors obtained by cross-validation.

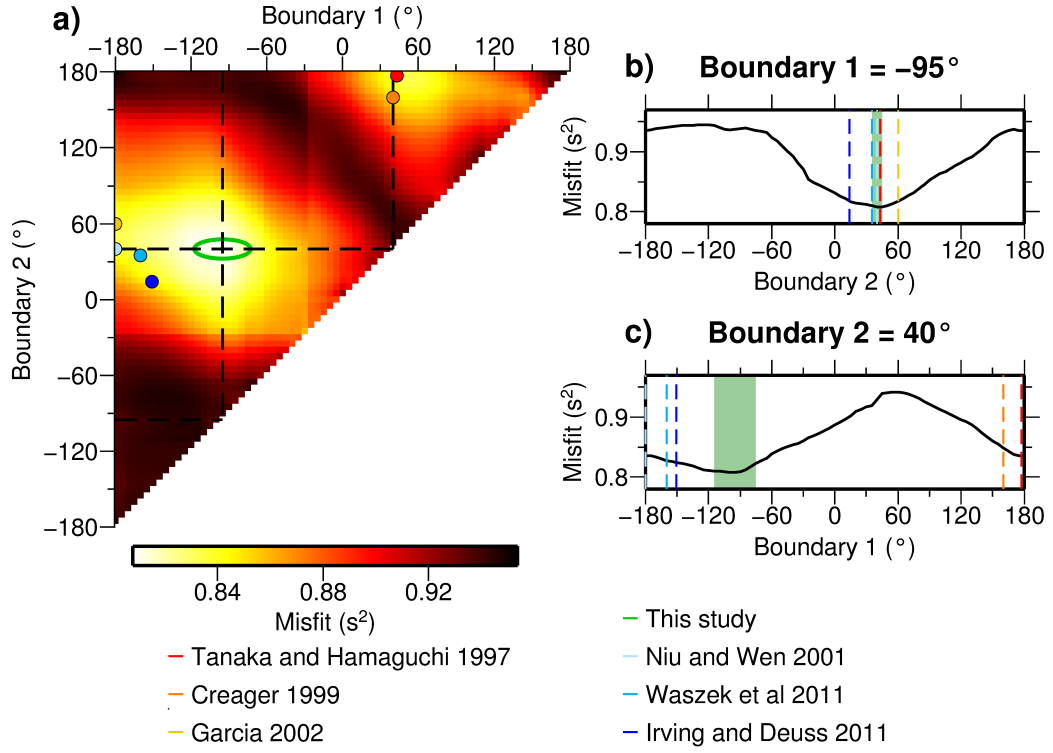


Figure 4: **a)** Misfit contour plot of boundary locations. Minimum misfit is at $40 \pm 5^\circ\text{E}$ and $95 \pm 20^\circ\text{W}$, with the error range marked by the green ellipse. **b, c)** Cross-section through minimum misfit boundary locations. Boundary locations are also plotted from previous studies.

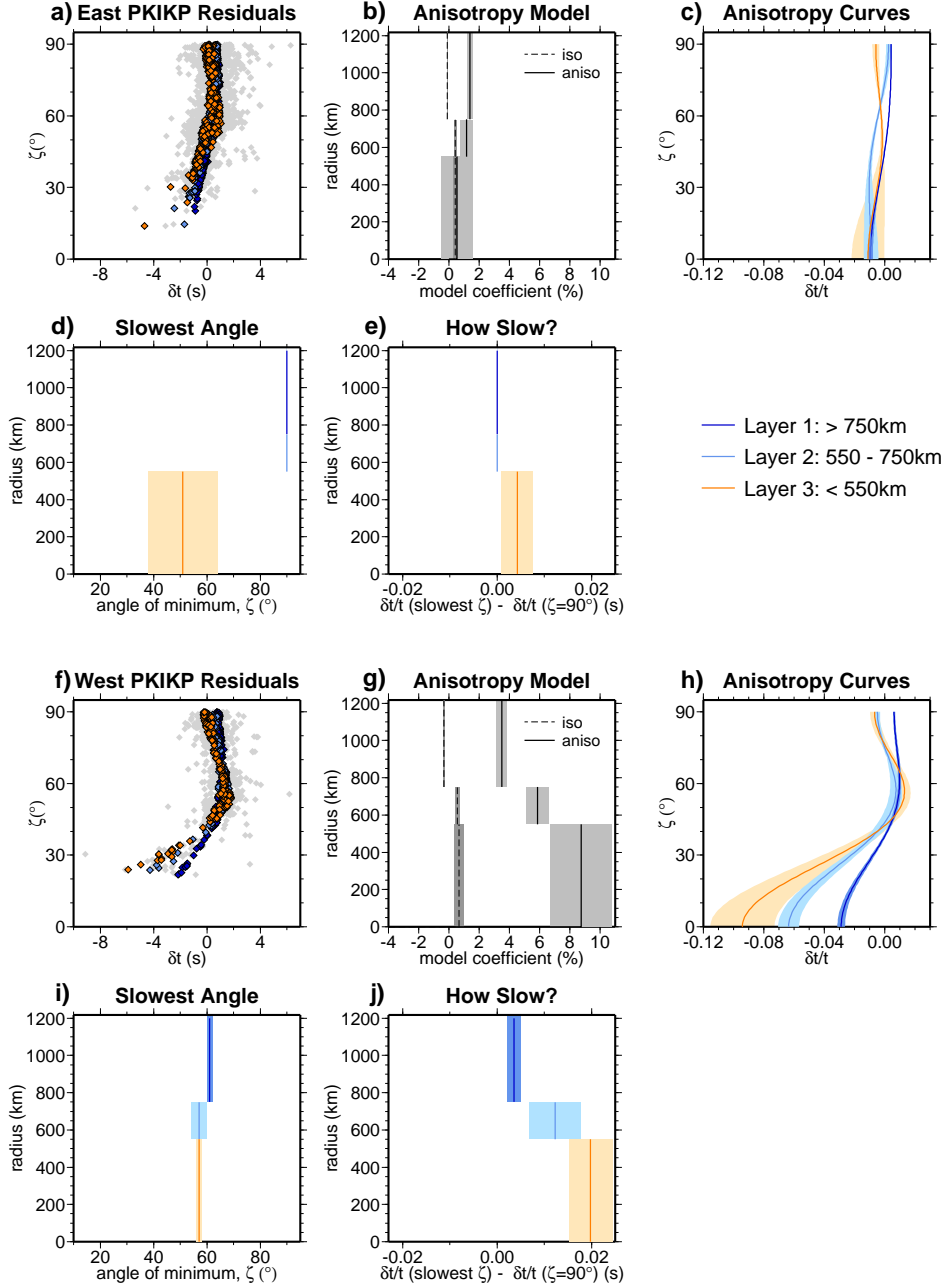


Figure 5: Anisotropy model for eastern (top) and western (bottom) hemispheres with hemisphere boundaries at 95°W and 40°E , and radial boundaries at 750 km and 550 km. **a)** Observed PKIKP travel time residuals (grey) and model predicted travel time residuals (colour) plotted for data with a turning position in the eastern hemisphere. **b)** Eastern hemisphere model isotropic (dashed) and anisotropic (solid) variations with respect to AK135. **c)** Anisotropy curves for eastern hemisphere. **d)** ζ for which the anisotropy curve is maximum. **e)** Difference between $\delta t/t$ for the slowest angle and the equatorial direction ($\zeta = 90^\circ$). **f,g,h,i,j)** for the western hemisphere. Shaded regions show errors obtained from cross-validation.

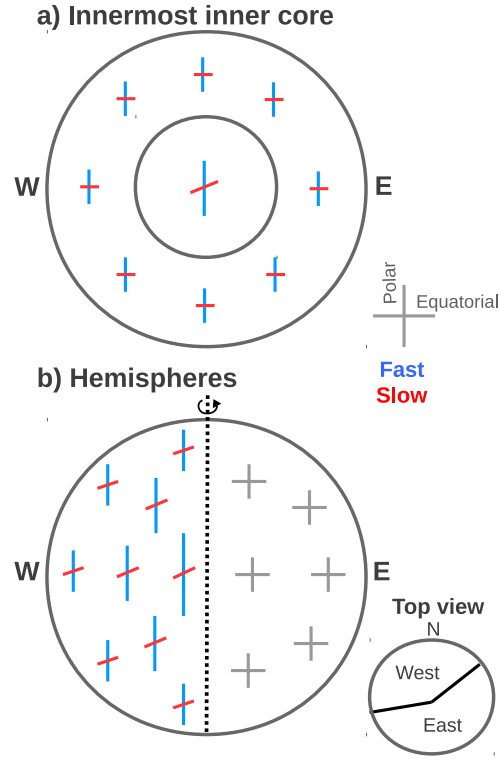


Figure 6: Schematic of inner core models with either **a)** an innermost inner core which has larger anisotropy and a slow direction at $\sim 56^\circ$ to the rotation axis or **b)** hemispherical variations where the eastern hemisphere is weakly anisotropic and the western hemisphere has high anisotropy that increases with depth, with a slow direction at $57\text{--}61^\circ$ throughout. Blue and red lines represent the fast and slow directions respectively. The length of the fast direction corresponds to the magnitude of anisotropy.

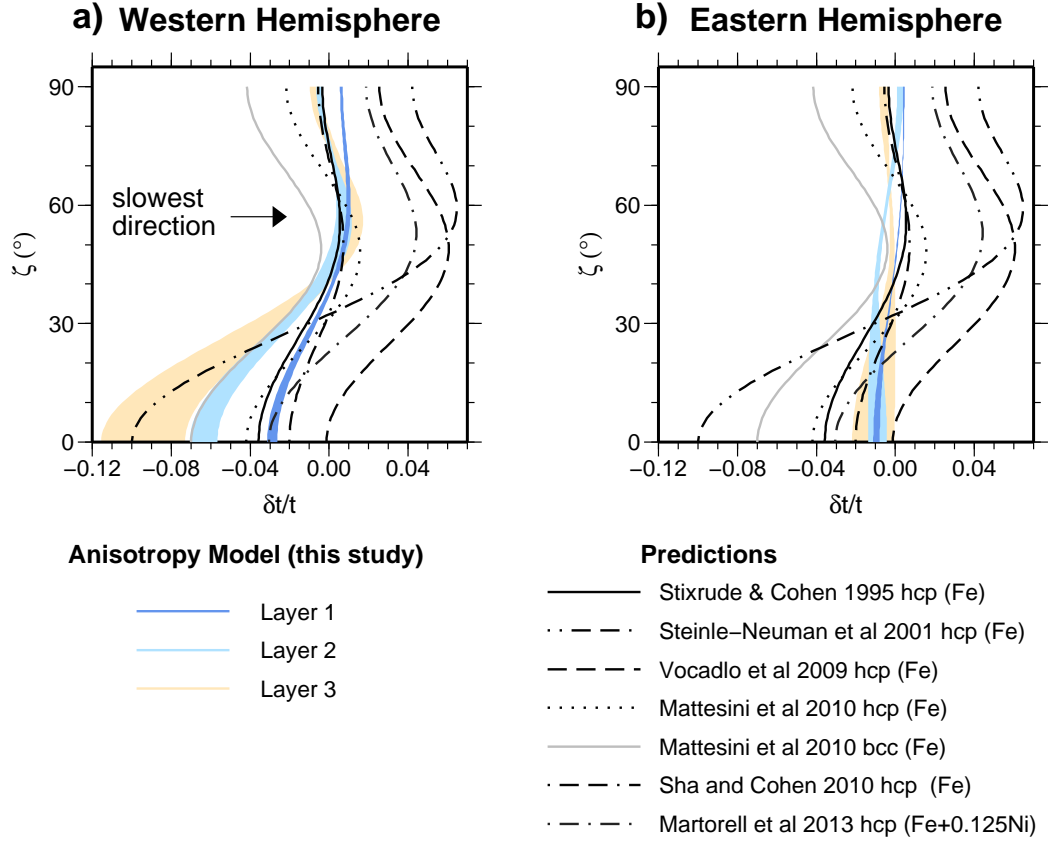


Figure 7: Anisotropy curves for **a)** western and **b)** eastern hemispheres. The anisotropy model from this study is plotted as in Figure 5c and 5h, with layer 1 above 750 km (dark blue), layer 2 from 550-750 km (light blue) and layer 3 below 550 km (orange). Also plotted are predicted anisotropy curves for different iron models at inner core conditions.